8. K. K. Likharev and A. B. Zorin, *J. Low Temp. Phys.* **59**, 347 (1985).
9. P. Lafarge *et al.*, *Z. Phys. B* **85**, 327 (1991).
10. M. W. Keller, J. M. Martinis, N. M. Zimmerman, A. H. Steinbach, *Appl. Phys. Lett.* **69**, 1804 (1996).
11. P. D. Dresselhaus, L. Ji, S. Han, J. E. Lukens, K. K. Likharev, *Phys. Rev. Lett.* **72**, 3226 (1994).
12. Y. Y. Wei, J. Weis, K. von Klitzing, K. Eberl, *Appl. Phys. Lett.* **71**, 2514 (1997).
13. M. J. Yoo *et al.*, *Science* **276**, 579 (1997).
14. For "standard" Al/AlO_x/Al junctions, the resistance is $R_J \sim 50$ kilohms and the capacitance $C_J \sim 0.2$ fF, so $1/2\pi R_J C_J \sim 16$ GHz. Alternatively, one can consider the rate at which electrons flow from drain to source in typical operation. This rate is just $f = I/e$, with I the current for which the modulation with gate is maximal, or approximately the threshold voltage over the minimum resistance of the SET, $I \sim e/C_\Sigma/4R_J$. Then this maximum tunneling rate is $f \sim 1/8R_JC_J$.
15. J. Petersson *et al.*, *Phys. Rev. B* **53**, 13272 (1996).
16. E. H. Visscher *et al.*, *Appl. Phys. Lett.* **68**, 2014 (1996).
17. B. Starmark, P. Delsing, D. B. Haviland, T. Claeson, in Extended Abstracts of the *6th International Superconductive Electronics Conference (ISEC '97)*, H. Koch and S. Knappe, Eds. (PTB, Berlin, 1997), vol. 2, p. 391.
18. If the characteristic impedance of the coaxial cable, Z_0, is equal to the amplifier's impedance (50 ohms), then the effective impedance of the cable plus amplifier is purely real and equal to Z_0.
19. J. Niemeyer, *PTB-Mitt.* **84**, 251 (1974); G. J. Dolan, *Appl. Phys. Lett.* **31**, 337 (1977).
20. R. J. Schoelkopf *et al.*, data not shown.
21. The voltage reflection coefficient is given by $(Z - Z_0)/(Z + Z_0)$, and when $Z = R_T \gg Z_0$, then the total reflected power is proportional to $1 - 4Z_0/R_T$. The minimum resistance of the SET (Fig. 2A) is $R_{min} \sim 200$ kilohms, and the maximum is much larger. So without the resonant circuit (C_{pad} and L), the expected fractional change in reflection would be only one part in 10^3. The measured "depth of modulation" for this device was $D \sim 4\%$, in good agreement with the expected value $D = 4(Q^2)Z_0/R_{min} \sim 3.7\%$, given the value of the quality factor of the resonator, $Q = \omega_0 L/Z_0$ of ~6.
22. We estimate that the ac drain-source voltage swing across the SET is ~0.3 mV (or $V/Q \sim 50$ μV outside the resonator), based on the applied power of ~50 pW.
23. G. S. Krivoy and H. Koch, *J. Appl. Phys.* **74**, 2925 (1993); G. S. Krivoy and V. A. Komashko, *Physica B* **165/166**, 83 (1990).
24. P. Wahlgren and R. J. Schoelkopf, in preparation.
25. These sidebands have been observed directly, by examining the RF output in front of the rectifying diode on a gigahertz spectrum analyzer.
26. The gate and all dc leads had several low-pass "powder" filters of the type described in J. M. Martinis, M. H. Devoret, and J. Clarke [*Phys. Rev. B* **35**, 4682 (1987)].
27. A. N. Korotkov, *ibid.* **49**, 10381 (1994); A. N. Korotkov, D. V Averin, K. K. Likharev, S. A. Vasenko, in *Single-Electron Tunneling and Mesoscopic Devices*, H. Koch and H. Lübbig, Eds. (Springer-Verlag, Berlin, 1992), p. 45.
28. A charge noise of 9×10^{-6} e/$\sqrt{\text{Hz}}$ has recently been obtained with a transimpedance amplifier and a superconducting Al SET in a narrow band near 4 kHz (B. Starmark, private communication).
29. For dc drain-source biases much larger than the threshold voltage, a small but linearly increasing component of the high-frequency noise could be seen, which was consistent with the expected values of the output current noise of the SET, $S_I \sim eI$.
30. R. H. Koch, D. J. Van Harlingen, J. Clarke, *Appl. Phys. Lett.* **38**, 380 (1981).
31. D. J. Van Harlingen, R. H. Koch, J. Clarke, *ibid.* **41**, 197 (1982); M. W. Cromar and P. Carelli, *ibid.* **38**, 723 (1981).
32. This statement only applies to the noise introduced by the detector (RF-SET). A true calculation of the counting errors will depend also on the statistics of the electron transmission process itself.
33. Y. Harada, D. B. Haviland, P. Delsing, C. D. Chen, T. Claeson, *Appl. Phys. Lett.* **65**, 636 (1994).
34. D. V. Averin and Yu. V. Nazarov, *Phys. Rev. Lett.* **65**, 2446 (1990).
35. V. Bouchiat, thesis, University of Paris (1997).
36. We thank K. K. Likharev, J. M. Martinis, R. D. Grober, and J. Zmuidzinas for useful discussions, J. Webber and R. Bradley of the National Radio Astronomy Observatory for making the HEMT amplifier available, and B. Starmark for experimental assistance and for sharing prepublication results. The samples were fabricated at the Swedish Nanometer Laboratory. Supported by NSF grants DMR-9216121 and DMR-9701427, and by ESPRIT (CHARGE 22953). P.W. wishes to acknowledge generous support from the Wallenberg Foundation.

29 December 1997; accepted 30 March 1998

Salts on Europa's Surface Detected by Galileo's Near Infrared Mapping Spectrometer

T. B. McCord, G. B. Hansen, F. P. Fanale, R. W. Carlson, D. L. Matson, T. V. Johnson, W. D. Smythe, J. K. Crowley, P. D. Martin, A. Ocampo, C. A. Hibbitts, J. C. Granahan, the NIMS Team

Reflectance spectra in the 1- to 2.5-micrometer wavelength region of the surface of Europa obtained by Galileo's Near Infrared Mapping Spectrometer exhibit distorted water absorption bands that indicate the presence of hydrated minerals. The laboratory spectra of hydrated salt minerals such as magnesium sulfates and sodium carbonates and mixtures of these minerals provide a close match to the Europa spectra. The distorted bands are only observed in the optically darker areas of Europa, including the lineaments, and may represent evaporite deposits formed by water, rich in dissolved salts, reaching the surface from a water-rich layer underlying an ice crust.

Europa is the second Galilean satellite outward from Jupiter. It is a lunar-sized object with a water-ice surface of relatively young geologic age (*1*, *2*). Its density and gravity field suggest a differentiated object with an Fe-rich core and silicate mantle underlying an ice-rich crust (*3*). The surface features and young age (*4*) suggest recent resurfacing, perhaps from a liquid water ocean existing between a relatively thin ice crust and the silicate mantle. Tidal heating has been suggested as the energy source to maintain an ocean in this relatively cold part of the solar system (surface temperatures on Europa range from 100 to 120 K) (*5*). The existence of heat and water plus organic molecules (*6*) has led many to speculate whether Europa's ocean might be an environment with the potential for sustaining life (*7*).

Ground-based telescope observations show that Europa exhibits a high visual albedo and other spectral reflectance characteristics in the 1- to 5-μm wavelength range that were reported to indicate the dominance (>85% by weight) of surface water ice or frost (or both) and only a few weight percent impurities, with the possible presence of iron-bearing minerals that reduce the visible brightness in some regions (*2*, *8*). In addition, forms of sulfur-rich species, including sulfur allotropes, SO, SO_2, and H_2S, have been suggested as impurities in Europa's surface on the basis of ultraviolet and visible spectroscopy and Voyager multispectral images (*9*, *10*). These sulfur-rich species are thought to be derived from materials sputtered from Io and carried to Europa by Jupiter's magnetosphere, although an interior origin has also been suggested (*10*).

Early observations by the Near Infrared Mapping Spectrometer (NIMS) (*11*) indicated a surface of almost pure water ice for a north polar region of Europa (*12*), consistent with the earlier interpretations of the telescopic spectra. Here, we discuss subsequent NIMS observations of Europa that indicate the presence of hydrated minerals. Water-related spectral features dominate the NIMS reflectance spectra in the 1- to 3-μm range for Europa (Fig. 1). These features are due to vibration modes and combinations of these modes for H–O–H (*13*) in ice or in association with hydrated species (*14*, *15*). The features include absorption bands centered near 1.04, 1.25, 1.5, and 2 μm; a weak temperature-sensitive ice band at 1.65 μm on the edge of the 1.5-μm feature (*16*); and the fundamental O–H stretching transition near 3 μm. Water is strongly absorbing longward of 2.5 μm and is mostly responsible for the low reflectance in this region for all icy Galilean satellites (*6*).

T. B. McCord, G. B. Hansen, F. P. Fanale, P. D. Martin, C. A. Hibbitts, Hawaii Institute of Geophysics and Planetology, University of Hawaii, Honolulu, HI 96822, USA.
R. W. Carlson, D. L. Matson, T. V. Johnson, W. D. Smythe, A. Ocampo, Jet Propulsion Laboratory, Pasadena, CA 91109, USA.
J. K. Crowley, U.S. Geological Survey, MS954, Reston, VA 20192, USA.
J. C. Granahan, STI Inc., Honolulu, HI 96813, USA.

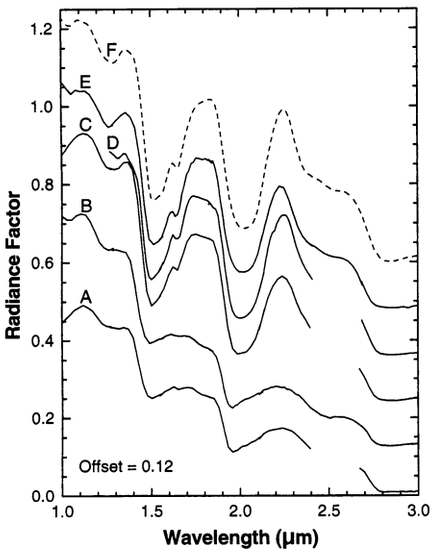

Fig. 1. Examples of NIMS reflectance spectra for Europa and Ganymede. The spectra grade from pure water ice (top) to Europa's least ice-like (bottom) and are offset vertically from each other by 0.12 in reflectance. The water features (for example, at 1.04, 1.25, 1.5, 2.0, and 2.8 μm) are prominent. Spectra A and C are each averages of 100 NIMS pixels from the TERINC (*29*) observation in the E6 orbit. Spectrum A is scaled by a factor of 1.3. Spectrum B is a 130-pixel average over a dark area in the NHILAT observation in the G1 orbit. Spectrum D is a full disk average (120 pixels) of Europa's leading hemisphere taken in the E11 orbit, scaled by a factor of 1.35. Spectrum E is from a few NIMS pixels measuring a very icy region of Ganymede. Spectrum F is pure water ice from a radiative transfer model with 20-μm grain size (*30*). Each curve shows a number of spectrum segment mismatched overlaps associated with NIMS's spectrum sampling process (*11*) and calibration uncertainties.

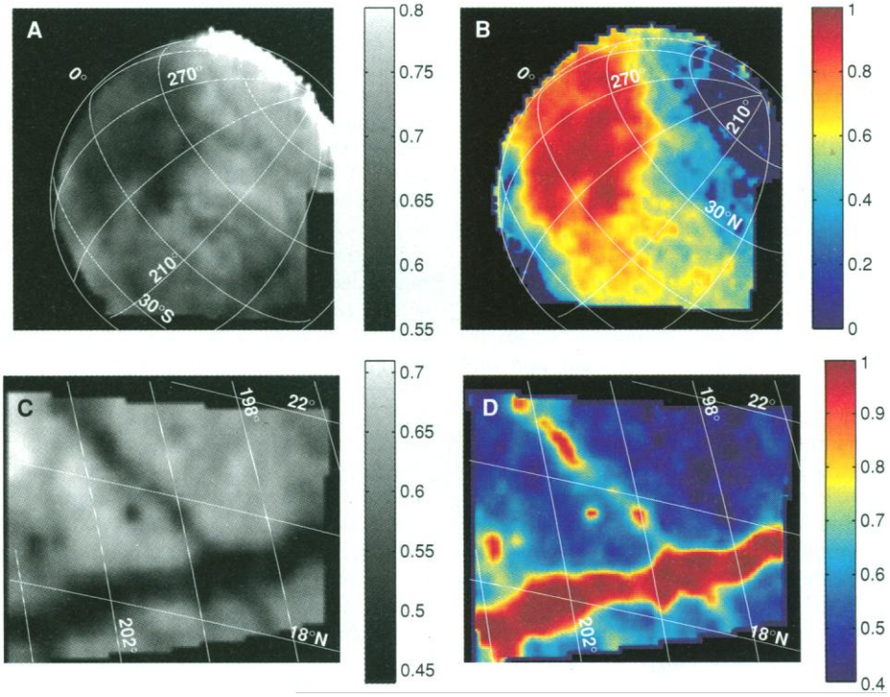

Fig. 2. (**A**) A near-hemispheric region of Europa at 77 km/pixel in the 0.7-μm NIMS passband. The gray scale bar indicates the approximate albedo for each pixel. (**B**) The relative concentrations of the nonice and ice-rich components of the surface, with dark red corresponding to the highest nonice concentration. The color scale bar indicates the relative amount of nonice component, where 1 = 100% nonice material. The nonice material is associated with the dark regions in (A). (**C**) High-resolution albedo image (~4 km/pixel) of a small region of Europa including a dark linea in the 0.7-μm passband from NIMS. (**D**) The distribution of the nonice component, with dark red being high nonice concentration. The nonice material is associated with the dark regions, including the linea.

At Europa's surface temperatures (100 to 120 K), H_2O is expected to exist as water ice, and ice is responsible for some of the spectral signatures (Fig. 1) (*6*, *8*). The NIMS data indicate that H_2O must also be present in other species besides ice to explain the asymmetric and broadened Europa absorption bands (*6*, *17*). Spectra from locations within each of the NIMS Europa data sets from Galileo orbits 1 to 11 that show the most distorted H_2O features were identified, and an average spectrum for each area was calculated (see example in Fig. 1). The average spectra for the most hydrate-rich areas were nearly identical, so they were averaged to produce a candidate generic hydrate spectrum.

This hydrate spectrum, a very ice-rich spectrum from portions of Ganymede, and spectra for areas on Europa with different (estimated) amounts of ice and nonice spectral characteristics were then used to estimate the proportions of ice and nonice material for each NIMS pixel and to map the distribution of the nonice material. The Ganymede nearly pure ice spectrum was used rather than the model ice spectrum in Fig. 1 because it was obtained with NIMS under similar conditions to the Europa observations and it may better represent the physically complex condition of the ice on Europa's surface. The nearly pure Ganymede ice and nearly pure Europa nonice material spectra shown in Fig. 1 and some other NIMS mixture spectra were used to calculate a series of synthetic spectra for intermediate mixtures that were compared with the spectrum for each NIMS pixel to estimate the proportions of ice and nonice materials present.

Although it is an oversimplification (*18*), this approach nevertheless resulted in distinctive maps of the nonice material that show that the nonice material is associated with the darker (lower visible albedo) regions, including the linea (Fig. 2) (*19*). In some areas, such as within some lineaments, there appears to be a near-perfect match to the nonice end-member spectrum, indicating less than about 1% ice. Furthermore, the spectra for the most ice-poor areas, even at the single pixel scale, are nearly identical, suggesting that the nonice material is of about the same composition everywhere so far studied.

The nonice end-member spectrum (Fig. 1) exhibits H_2O absorptions, especially in the 1.5- and 2.0-μm regions, that are highly distorted compared with water ice features, and the continuum is increasingly depressed toward longer wavelengths. Inspection of the H_2O spectral features in the nonice material indicates (*14*, *15*) that (i) the H_2O molecule has to be present (the OH functional group alone is not sufficient to explain the absorption bands because OH has no 2.0-μm absorption), (ii) the H_2O molecule is active spectrally, indicating abundant water in the mineral because its features are expressed so strongly in the spectrum, and (iii) the H_2O molecules are relatively closely bound to the host molecule in numerous slightly different bonding configurations to account for the strong and multiple distorting effects the host electric potential has on the H_2O bonding energy. Slightly hydrated mineral species generally show narrower H_2O absorption features because of fewer water molecules per formula unit, fewer sites of different potentials, and therefore less spreading of each band's energies. Thus, the candidate minerals are likely to be of the form mineral·xH_2O, where x is large and the H_2O is incorporated in the crystal structure as opposed to being adsorbed.

Spectral libraries (*15*, *20*) contain only a

few spectra of hydrated minerals resembling Europa's spectra. Nonhydrated and hydroxylated minerals do not exhibit similar spectral features. Hydrated clay minerals have been suggested as candidate materials for Europa's dark regions (*8*, *21*), but their spectral signatures differ from Europa's in several ways. The spectra for clays show additional absorptions in the 2.2- to 2.4-μm range, due to metal–OH (for example, Fe, Mg, and Al) absorptions (*14*, *20*), which are not present in Europa's spectra. These features can be suppressed in mixtures containing other absorbers, which reduce the reflectance and thus the spectral contrast. In Europa's case, however, they should be evident because some locations seem to be nearly 100% hydrated mineral and the reflectance remains high (≥50% of 1-μm reflectance) in the 2.2- to 2.4-μm region. Also, clays generally have more symmetric and narrower H_2O features positioned at shorter wavelengths than those observed in the Europa nonice spectrum. Clays also lack the decreasing continuum reflectance toward longer wavelengths (*14*, *20*) typical of Europa's nonice material.

The class of minerals whose spectra most closely resemble those of Europa is the hydrated salts. Of these, sulfates, carbonates, and borates have spectra (*15*, *20*) that are most consistent with Europa's nonice spectra. Borates seem unlikely given the low solar abundance of boron and the generally complex spectra shown by many borate minerals (*15*, *20*). From our study of available spectra, heavily hydrated carbonates and sulfates appear to be the better candidates. For example, natron ($Na_2CO_3 \cdot 10H_2O$) has a reflectance decrease toward longer wavelengths similar to that of Europa's nonicy regions (Fig. 3), but the 1.45- and 2.0-μm water features are a little more symmetric and less distorted at their core than Europa's. $MgSO_4 \cdot xH_2O$ is also a likely candidate with hexahydrite ($MgSO_4 \cdot 6H_2O$) and epsomite ($MgSO_4 \cdot 7H_2O$) having the most similar spectra (Fig. 3). Other sulfate features at longer wavelengths within the NIMS spectral range in these heavily hydrated materials are masked by stronger H_2O features (*5*). Other Mg sulfates with $x < 6$, such as pentahydrite ($MgSO_4 \cdot 5H_2O$), do not exhibit sufficiently distorted water bands to match Europa's spectrum. Other cations, such as Na, also occur in this structure with Mg (*22*), but they should not substantially change H_2O bonding energies and thus the spectral features analyzed here. Mixtures of carbonate and sulfate minerals provide even better matches to Europa's spectrum than the individual minerals. A mixture of salts is reasonable given that the nonice material spectrum is almost identical everywhere observed, implying a source of approximately uniform composition on a hemispherical scale.

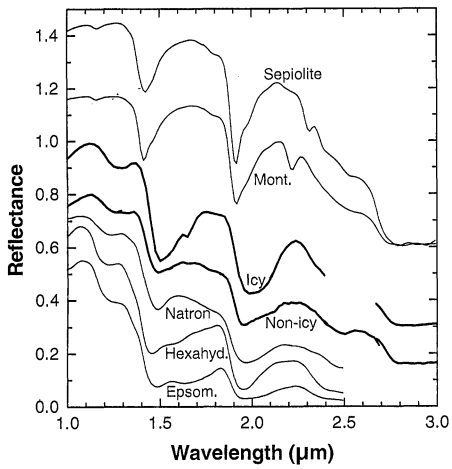

Fig. 3. Reflectance spectra from the Galileo NIMS instrument of Europa's nonicy and icy areas are averaged and scaled to qualitatively compare with reflectance spectra of possible surface minerals. The NIMS spectra are offset by 0.15 (nonicy) and 0.3 (icy) and are plotted with heavier lines. The hydrated sulfate and carbonate minerals hexahydrite (Hexa.) [$MgSO_4 \cdot 6H_2O$], epsomite (Epsom.) ($MgSO_4 \cdot 7H_2O$), and natron ($Na_2CO_3 \cdot 10H_2O$) show similar features and are the prime candidates (including in mixtures) for the material composing much of the nonice portion of the surface. No offset is used for these spectra. Hydrated clay minerals such as sepiolite [$Mg_4Si_6O_{15}(OH)_2 \cdot H_2O$] and montmorillonite (Mont.) [$(Na,Ca)_{0.33}(Al,Mg)_2Si_4O_{2}10(OH)_2 \cdot nH_20$] do not have the broadened water features found for Europa. Furthermore, clays have metal–OH absorptions in the 2.2- to 2.4-μm region that do not occur for Europa. The sepiolite and montmorillonite spectra are each offset 0.6.

There are other effects that could refine our interpretations of Europa's spectra. There may be temperature-induced spectral differences between ambient laboratory and Europa observations. One effect of colder temperatures on these H_2O features in hydrated minerals would be a narrowing of the bands similar to that seen in water-ice spectra (*23*). This phenomenon is sufficiently understood and does not alter our analysis. The particle size of materials can affect the absolute and relative strengths of absorptions in the spectrum of individual samples by changing the distance a photon travels through a grain, and thus the absorption probability, between scattering boundaries. However, the shape and symmetry of the absorption band do not change other than to become stronger or weaker, except in the case of a composite of overlapping bands with large differences in absorption strengths. This fact and our investigations over the limited available range of particle sizes for salt minerals suggest that it is unlikely that differences in grain size effects can alter our interpretations.

Hydrated salt minerals are usually formed on Earth by evaporation of brines on the surface and precipitation of the salts leaving a lag deposit of salt crystals (*24*). If there is a liquid ocean below the ice crust on Europa, there must be heat generated in the interior of Europa to maintain the ocean. There may be volcanic or hydrothermal activity and dissolution of ions into the ocean, as occurs on Earth's ocean floor. If an ocean brine within Europa were extruded onto the surface, it would encounter a vacuum and a temperature < 125 K. The exposed brine would be concentrated by a number of mechanisms, including flash evaporation, freezing, sublimation, and sputtering, leaving some crystallized salts as an evaporite-like deposit. Hydrated magnesium sulfate, common in evaporite deposits on Earth, is highly soluble in water and is found in aqueous-altered meteorites (*25*). Also, sodium carbonates, such as natron, are found in large quantities in terrestrial evaporite deposits derived primarily from carbonic acid weathering of volcanic rocks.

Models of an evolving Europa that use initial carbonaceous chondrite composition predict large amounts of hydrated $MgSO_4$ (*25*), and recent experiments dissolving meteorites in water produced hydrated $MgSO_4$-rich leachates (*26*). The NIMS results seem to confirm these models. Kargel (*25*) suggested that the state of hydration on Europa may be as high as $\cdot 12H_2O$, substantially more that the $\cdot 7H_2O$ maximum easily produced at room temperatures. Greater hydration will tend to further broaden and distort the H_2O absorptions, which may allow an even better match to Europa's spectrum.

The occurrence of evaporite minerals in general and carbonates in particular on Europa's surface would place important constraints on chemical processes in the interior and provide important ions that could be supportive of life in the ocean (*27*). For example, if Europa's ocean is enriched in dissolved carbonate species, this would require an alkaline water chemistry such as would exist with high CO_2 concentrations. A similar ocean composition has been proposed as the setting for the development of primitive life on Earth (*28*). For Earth, the CO_2 was in the early atmosphere. For Europa, the ice crust may trap CO_2 released by heating of the interior.

REFERENCES AND NOTES

1. B. A. Smith *et al.*, *Science* **206**, 927 (1979); B. K. Lucchitta and L. A. Soderblom, in *Satellites of Jupiter*, D. Morrison, Ed. (Univ. of Arizona Press, Tucson, AZ, 1982), pp. 521–555; M. C. Malin and D. C. Pieri, in *Satellites*, J. A. Burns and M. S. Matthews, Eds. (Univ. of Arizona Press, Tucson, AZ, 1986), pp. 689–717; M. H. Carr *et al.*, *Lunar Planet. Sci.* **XXVIII**, 207 (abstr.) (1997).
2. C. B. Pilcher, S. T. Ridgway, T. B. McCord, *Science* **178**, 1087 (1972).
3. J. D. Anderson, E. L. Lau, W. L. Sjogren, G. Schubert, W. B. Moore, *ibid.* **276**, 1236 (1997).
4. M. H. Carr *et al.*, *Nature* **391**, 363 (1998).
5. P. M. Cassen, R. T. Reynolds, S. J. Peale, *Geophys.*

Res. Lett. **6**, 731 (1979); P. M. Cassen, S. J. Peale, R. T. Reynolds, *ibid.* **7**, 987 (1980); S. W. Squyres, R. T. Reynolds, P. M. Cassen, S. J. Peale, *Nature* **301**, 225 (1983).
6. T. B. McCord *et al.*, *Science* **278**, 271 (1997); T. B. McCord *et al.*, *Eos (Spring Suppl.)* **78**, S202 (abstr.) (1997); T. B. McCord *et al.*, *J. Geophys. Res.* **103**, 8603 (1998).
7. R. T. Reynolds, S. W. Squires, D. S. Colburn, C. P. McKay, *Icarus* **56**, 246 (1983).
8. The main water-ice absorptions were reported at 3.0, 2.0, 1.5, 1.25, and 1.04 μm. For example, G. P. Kuiper, in *The Solar System, 3, Planets and Satellites*, G. P. Kuiper and B. M. Middlehurst, Eds. (Univ. of Chicago Press, Chicago, IL, 1961), pp. 305–306; V. I. Moroz, *Trans. Soviet. Astron. A. J.* **9**, 999 (1965); T. V. Johnson and T. B. McCord, *Astrophys. J.* **169**, 589 (1971); H. H. Kieffer and W. D. Smythe, *Icarus* **21**, 506 (1974); J. B. Pollack *et al.*, *ibid.* **36**, 271 (1978); R. N. Clark, *ibid.* **44**, 388 (1980); *J. Geophys. Res.* **86**, 3087 (1981); *Icarus* **49**, 244 (1982); T. V. Johnson *et al.*, *J. Geophys. Res.* **88**, 5789 (1983). See W. M. Calvin, R. N. Clark, R. H. Brown, and J. R. Spencer [*J. Geophys. Res.* **100**, 19041 (1995)] for the most recently reported data and a review.
9. A. L. Lane, R. M. Nelson, D. L. Matson, *Nature* **292**, 38 (1981); R. M. Nelson *et al.*, *Icarus*, **72**, 358 (1986); R. E. Johnson, M. L. Nelson, T. B. McCord, J. C. Gradie, *ibid.* **75**, 423 (1988); M. K. Pospieszalska and R. E. Johnson, *ibid.* **78**, 1 (1989); N. J. Sack, R. E. Johnson, J. W. Boring, R. A. Baragiola, *ibid.* **100**, 534 (1992).
10. K. F. Noll, A. Weaver, A. M. Gonnella, *J. Geophys. Res.* **100**, 19057 (1995).
11. The Galileo NIMS began spectrometric observations of the Galilean satellites in June 1996. The NIMS covers the wavelength (λ)range 0.7 to 5.2 μm with up to 408 spectral channels and a resolving power of 40 to 200 (λ/Δλ). The instrument's instantaneous field of view is 0.5 mrad, giving a spatial resolution (pixel size) of, for example, 5 km at 10,000-km distance. The spectra are calibrated to units of reflectance at the specific geometry of the observation compared with the reflectance of a perfectly diffusing (Lambert) surface with the use of the solar spectrum and a combination of ground and in-flight NIMS measurements of calibration targets. See R. W. Carlson, P. R. Weissman, W. D. Smythe, J. C. Mahoney, and the NIMS Science and Engineering Team [*Space Sci. Rev.* **60**, 457 (1992)] for a description of the NIMS instrument.
12. R. W. Carlson *et al.*, *Science* **274**, 385 (1996).
13. N. Ockman, *Adv. Phys.* **7**, 199 (1958); W. M. Irvine and J. B. Pollack, *Icarus* **8**, 324 (1968); P. V. Hobbs, *Ice Physics* (Clarendon, Oxford, UK, 1974); S. G. Warren, *Appl. Opt.* **23**, 1206 (1984).
14. For example, G. R. Hunt, J. W. Salisbury, C. J. Lenhoff, *Mod. Geol.* **3**, 1 (1971); *ibid.* **4**, 85 (1973).
15. J. K. Crowley, *J. Geophys. Res.* **96**, 16231 (1991).
16. U. Fink and H. P. Larson, *Icarus* **24**, 411 (1975).
17. R. W. Carlson and the NIMS Team, paper presented at the Workshop on Remote Sensing of Planetary Ices: Earth and Other Solid Bodies, Flagstaff, AZ, 11 to 13 June 1997; R. W. Carlson, paper presented at the Annual Meeting of the Geological Society of America, Salt Lake City, UT, 22 October 1997.
18. This approach ignores many factors affecting the details of reflectance spectra, such as particle size and multiple nonlinear scattering. It is used here to demonstrate some outstanding fundamental properties in a rapid and simple manner.
19. T. B. McCord *et al.*, *Eos (Fall Suppl.)* **78**, F407 (abstr.) (1997); T. B. McCord *et al.*, *Lunar Planet. Sci.* **XXIX**, 1560 (abstr.) (1998). A band-minimum (rather than total band shape) map for one Europa area also was presented by J. C. Granahan *et al.* [*Eos (Fall Suppl.)* **78**, F417 (abstr.) (1997)].
20. For example, J. K. Crowley, *Remote Sensing Environ.* **44**, 337 (1993); *Econ. Geol.* **91**, 622 (1996); R. N. Clark, G. A. Swayze, A. Gallagher, T. V. V. King, W. M. Calvin, *U.S. Geol. Surv. Open File Rep. 93-592* (1993). See these references for descriptions of various minerals.
21. J. C. Granahan *et al.*, *Bull. Am. Astron. Soc.* **29**, 982 (abstr.) (1997); F. P. Fanale *et al.*, in preparation.
22. R. V. Gaines, H. C. W. Skinner, E. E. Foord, B. Mason, A. Rosenzweig, *Dana's New Mineralogy* (Wiley, New York, ed. 8, 1997).
23. W. Hagen, A. G. G. M. Tielens, J. M. Greenberg, *Chem. Phys.* **56**, 367 (1981); W. Hagen and A. G. G. M. Tielens, *Spectrochim. Acta* **38A**, 1089 (1982); W. M. Grundy and B. Schmitt, *J. Geophys. Res.*, in press.
24. For example, L. A. Hardie, *Geochim. Cosmochim. Acta* **32**, 1279 (1968).
25. F. P. Fanale, T. V. Johnson, D. L. Matson, in *Planetary Satellites* (Univ. of Arizona Press, Tucson, AZ, 1977), pp. 379–405; J. S. Kargel, *Icarus* **94**, 368 (1991).
26. F. P. Fanale *et al.*, *Lunar Planet. Sci.* **XXIX**, 1248 (abstr.) (1998).
27. R. Y. Stanier *et al.*, *The Microbial World* (Prentice-Hall, Englewood Cliffs, NJ, 1986), pp. 22–23.
28. For example, see S. Kempe, J. Kazmierczak, E. T. Degens, in *Origin, Evolution and Modern Aspects of Biomineralization in Plants and Animals*, R. E. Crick, Ed. (Plenum, New York, 1989), pp. 29–43.
29. NIMS observations are named for the primary satellite target, the number of the orbit around Jupiter, and the name of the target area on the satellite, for example, E6TERINC = Europa, 6th orbit, Terra Incognito.
30. The water frost albedo model used is from W. J. Wiscombe and S. G. Warren [*J. Atmos. Sci.* **37**, 2712 (1980)], and the optical constants used are described by G. B. Hansen, T. B. McCord, and the NIMS Team [*Lunar Planet. Sci.* **XXVIII**, 505 (abstr.) (1997)].
31. This work was supported in part by the NASA Galileo Project. This is SOEST publication 4622 and HIGP publication 987.

18 February 1998; accepted 13 April 1998

Viscosity of Oceanic Asthenosphere Inferred from Remote Triggering of Earthquakes

Fred F. Pollitz, Roland Bürgmann, Barbara Romanowicz

A sequence of large interplate earthquakes from 1952 to 1965 along the Aleutian arc and Kurile-Kamchatka trench released accumulated stresses along nearly the entire northern portion of the Pacific Plate boundary. The postseismic stress evolution across the northern Pacific and Arctic basins, calculated from a viscoelastic coupling model with an asthenospheric viscosity of 5×10^{17} pascal seconds, is consistent with triggering of oceanic intraplate earthquakes, temporal patterns in seismicity at remote plate boundaries, and space-based geodetic measurements of anomalous velocity over an area 7000 by 7000 kilometers square during the 30-year period after the sequence.

Stress pulses travelling away from an earthquake source area effectively transmit the local stress changes associated with the earthquake to a much larger area as the ductile sublithospheric channel gradually yields with time (*1*–*4*). Several studies have applied such a model to the continental lithosphere, where predictions may be readily compared with geodetic observations [for example, see (*3*–*7*)]. There have also been a few applications suggestive of stress diffusion through the ocean basins (*1*, *2*, *8*). Here we evaluate postseismic stress evolution driven by large subduction events that occurred along the Aleutian and Kurile-Kamchatka trenches from 1952 to 1965 (Fig. 1A) and use the inferred correlation with seismicity to estimate the viscosity of the oceanic asthenosphere. The subduction earthquakes have total seismic moment exceeding 1000×10^{20} N·m and are by far the largest involving the Pacific Plate to have occurred during the period 1950–1970 (*9*). Moreover, each of them occurred on subduction interfaces that had experienced smaller events on time scales of 20 to 90 years but no comparable large ruptures for at least the past 200 years (*10*). Because these events involve only the Pacific–North America plate boundary, stress changes may be evaluated without any significant complications over the entire Pacific basin as well as the Arctic basin (on the North American Plate). We specified the elastic deformation associated with these earthquakes in terms of the fault planes and slip directions shown in Fig. 1A and source parameters from (*11*). We also included a few smaller but significant events with total seismic moment of $\sim 150 \times 10^{20}$ N·m: thrust events along the Kurile/Bonin arc in 1958, 1963, 1968, 1969, 1972, 1973, and 1978, and the 1986 Andreanof Islands earthquake along the Aluetian arc (*12*).

We constructed a rheology appropriate for the oceanic lithosphere from the seismic structure determined by Gaherty *et al.* (*13*) and then calculated postseismic gravitational-viscoelastic relaxation on a grid covering the northern Pacific and Artic basins (*4*). The model implies that for an asthenospheric viscosity of $\eta = 5 \times 10^{17}$ Pa·s, the leading edge of the stress pulse passed by the Juan de Fuca plate in 1975 and California in 1985 (the southward-propagating blue region in Fig. 1). The dispersive character of the propagating stress pulse is such that

F. F. Pollitz and R. Bürgmann, Department of Geology, University of California, Davis, Davis, CA 95616, USA. B. Romanowicz, University of California Seismological Laboratory, 475 McCone Hall, Berkeley, CA 94720, USA.